Transient stress evolution of the long-term slow slip cycle initiates the 2014 M_w7.3 Guerrero earthquake

Duo Li[1,*] **and Alice-Agnes Gabriel**[2,1]

[1]Department of Earth and Environmental Sciences, Ludwig-Maximilians-Universität München, Munich, Germany
[2]Institute of Geophysics and Planetary Physics, Scripps Institution of Oceanography, University of California San Diego, La Jolla, USA
[*]dli@geophysik.uni-muenchen.de

ABSTRACT

Transients of aseismic fault slip, slow-slip events (SSEs), have been observed in spatial and temporal proximity to the initiation of megathrust earthquakes. However, the underlying physics potentially connecting a preceding SSE to earthquake rupture remains to be determined. Here, we link 3D observation-driven slow-slip cycle models with dynamic rupture simulations of the 2014 M_w7.3 Guerrero, Mexico earthquake across the geometrically complex flat-slab Cocos plate. Our physics-based models reproduce key regional geodetic and teleseismic observations on timescales ranging from decades to seconds. We find that accelerating SSE fronts transiently increase shear stress at the down-dip end of the seismogenic portion of the megathrust. The stresses cast by the 2014 M_w 7.6 SSE are significantly larger than those during the three previous episodic SSEs, and can dynamically initiate earthquake rupture. We show that in addition to the transient stresses caused by SSEs, megathrust asperities explain the observed complexities in the coseismic energy release and static surface displacements. We conclude that it is crucial to jointly analyze the long- and short-term interactions of SSEs and megathrust earthquakes across several (a)seismic cycles. Our study has important implications for identifying earthquake precursors and understanding megathrust faulting processes.

1 Introduction

Transient quasi-static fault deformation, slow-slip events (SSEs), or silent earthquakes have been observed at convergent plate boundaries[1–5] and at large continental faults, e.g., the San Andreas fault[6,7]. SSEs may be accompanied by low-frequency seismic radiation, including non-volcanic tremors (NVTs), low-frequency earthquakes (LFEs), and very-low-frequency earthquakes (VLFEs)[8,9]. SSEs usually slip 10-100 times faster than the tectonic loading and last from days to years at depths close to the brittle-ductile transition[1,4,5]. The physical mechanisms underlying SSEs and their interaction with earthquakes are debated[10]: The spatial viability of both fast and slow earthquakes on plate-boundary faults has been attributed to several factors, including structural and material heterogeneity[11–15], rheological variability with depth[16,17] and fluid migration within oceanic sedimentary layers[18,19].

The kinematic migration patterns of off-shore aseismic slip are often challenging to constrain due to the lack of dense geodetic observations. Sequences of foreshocks and migrating seismicity before large events such as the 2011 Tohoku-Oki earthquake have been interpreted as proxies for aseismic fault slip and as potential long-term precursory signals of megathrust earthquake nucleation processes[20]. Other observations of possible precursory signals include the acceleration of a M_w 6.5 slow slip event that was recorded by the land-based GPS stations eight months before the 2014 M_w 8.1 North Chile earthquake[21].

Whether transient slow slip can serve as a universal precursor of eminent megathrust earthquake initiation is essential for seismic and tsunami hazard assessments in metropolitan margins[10,22–24]. However, the spatial and temporal interactions between slow and fast earthquakes, specifically the potential of slow-slip triggering megathrust earthquakes, remain enigmatic. Due to the observational challenges associated with the large variability of space and time scales, physics-based models are indispensable to illuminate the physics and in-situ fault properties rendering SSE triggering of large earthquakes plausible.

On April 18, 2014, a M_w 7.3 megathrust earthquake struck the coast of Mexico at the western edge of the Guerrero Gap, which had experienced no significant seismic events since 1911[25,26]. Geodetic inversions suggest that long-term slow-slip cycles have accommodated most of the plate convergence on the sub-horizontal oceanic slab between 20-45 km depth in Guerrero[25–27] (Fig. 1a). In addition to long-term SSEs, transient bursts of short-term low-frequency earthquakes and non-volcanic tremors have been detected at different depths along the slab[18,28–30]. Slow-slip and slow earthquakes have been attributed to the elevated pore fluid pressure associated with an ultra-low velocity layer atop the subducting plate derived from dense-array seismic imaging[31]. Recent off-shore seismic observations have revealed a combination of earthquakes, aseismic and creeping deformation, suggesting the existence of multiple asperities across the slab interface[32]. Considering the unique slip characteristics of the Guerrero Gap, the initiation of the 2014 $M_\mathrm{w}7.3$ earthquake has been related to the accumulated static Coulomb stress changes cast by an ongoing slow-slip event below 20 km depth that eventually accumulated an equivalent moment magnitude of $M_\mathrm{w}7.6$ on the megathrust interface[27,33].

In this study, we present 3D numerical models of the dynamic rupture of the 2014 $M_\mathrm{w}7.3$ Guerrero earthquake, linked to 3D episodic slow-slip cycles under long-term tectonic loading, ensuring consistent stress states across the fault interface. Physics-based models of earthquake initiation, propagation, and arrest require choices regarding the pre-existing state of stress and fault strength governing frictional sliding[34–39]. Our SSE cycle and dynamic rupture models account for the same geophysical and geological observational inferences, such as the regional slab geometry, elevated pore fluid pressure, and depth-dependent frictional strength constrained from laboratory experiments and thermal modeling. We bridge time scales from decades governing four episodes of long-term SSEs to fractions of seconds during earthquake rupture within the Guerrero Gap using the SSE cycle results to inform the dynamic earthquake rupture scenario models. The modeled, observationally constrained, transient stress evolution of the 2014 SSE event can lead to spontaneous co-seismic failure in the hypocentral region of the Guerrero earthquake. However, the episodic increase in shear stress caused by the three preceding SSEs, which correspond to the 2002, 2006, and 2009-2010 SSEs, remains too small compared to the high static fault strength required to match observations in the dynamic rupture model. We also find that, in addition to SSE-induced stress heterogeneity, the complex propagation and arrest of the Guerrero earthquake require pre-existing variable friction properties. Our study provides a mechanically self-consistent model for slow-slip triggered megathrust earthquakes and has important implications for the interaction between earthquakes and slow-slip in subduction zones and at large continental faults worldwide.

2 Results

The 2014 M_{w} 7.6 slow-slip event on the curved and fluid-rich flat slab of the Guerrero Gap

We model episodic slow-slip cycles spontaneously emerging under long-term geological loading along the curved slab interface of the Guerrero Gap (see Fig. 1b), Methods: "Quasi-dynamic simulation of long-term slow slip cycles"). The long-term tectonic loading, which accumulates fault shear stresses, is balanced by the fault strength which is defined from a laboratory-derived rate-and-state friction law. We constrain the fault frictional parameters by combining laboratory experiments on wet gabbro gouges[40]with a 2D steady-state thermal model constrained by P-wave seismic tomography[41]. We extend a previous model that focused on the deeper part (10 km - 60 km depth) of the slab covering episodic SSEs only[42]. Here, we consider the geometrically complex slab up to the trench and thus include the entire seismogenic zone (5 km - 60 km depth). We account for elevated pore fluid pressure atop the oceanic plate which locally reduces fault strength and eventually leads to episodic slow-slip emerging between depths of 20 km and 45 km (Fig.S1). This elevation of pore fluid pressure has been suggested based on the seismically inferred high Vp/Vs ratios in central Mexico[31] as well as in other subduction zones[2,43].

We model cycles of long-term SSEs that occur repeatedly every four years. Fig. 2 shows exemplary snapshots of the fault slip rate in the modeled scenario of the 2014 SSE. Each SSE episode lasts for up to 12 months[26] and reaches a peak slip rate of up to 10^{-6} m/s (Fig. 2a,c,e). Our numerical results match the region-specific source characteristics of long-term SSEs inferred from geodetic inversion using the regional GPS network[27] (Supplementary Table S1). We attribute the good match of the first-order SSE characteristics to the realistic flat slab geometry and assumed near-lithostatic pore fluid pressure[14,42]. We select four sequential SSE episodes of our model, closely corresponding to the four geodetically recorded events in 2002, 2006, 2009-2010, and 2014. We calculate the horizontal and vertical components of synthetic surface displacements at regional GPS stations and compare them with geodetic inversions[26,44]. The comparison between the synthetic and observed GPS vectors during the 2014 SSE is shown in Figs. 2g and 2h and for the three earlier SSE episodes in Figs. S5. All modeled SSE events yield good agreement with geodetic observations, although only dip-slip is considered in our simulations[14].

The 2014 SSE initiates simultaneously at the eastern and western edges of the Guerrero Gap at a depth of 40 km. Both slip fronts migrate towards the center at a rate of 0.5 km/day (Fig. 3). The megathrust slips at a higher rate after the coalescence of the migrating fronts in the center, and the SSE then bilaterally propagates across the entire fault between 25 km and 40 km depth. However, we observe no immediate coseismic slip nucleating upon coalescence of the SSE fronts (between a depth of 20-45 km). This is different from the results of earlier 2D planar fault simulations[45] but in agreement with recent on- and off-shore observations that find no evidence of coseismic rupture due to collapsed slow-slip migrating fronts in the Guerrero Gap[32].

Fig. 3 shows the time-dependent evolution of the on-fault shear-to-effective-normal traction ratio and along-strike migration speed during the cycle of all four SSEs. During the quasi-periodic emergence of the SSEs, we find that fault shear tractions overall increase down-dip of the seismogenic zone (below a depth of 20 km). However, this increase is not steady and varies considerably with the acceleration of the migrating slip fronts. The space-time evolution of the traction ratio, defined as the shear over effective normal stress during the modeled transient slip, is shown in Figs. 2b,d and f. Here, the traction ratio increases gradually from down-dip (30 km depth) to up-dip (20 km depth) and eventually reaches 0.64 in the hypocentral area of the 2014 M_w7.3 earthquake at a depth of 22 km, which is slightly shallower than that inferred by the USGS (Figs. 2f and 3a).

The migrating 2014 SSE front moves slowly until day 267 and accelerates to 3.0 km/day at day 317 (Fig. 3b). This acceleration, associated with rapid strain energy release, eventually increases shear stress at the down-dip end of the seismogenic zone in our model (see Fig. 3c and Movie S2). The migration speed can vary depending on the temporal stress evolution during the modeled SSE, which results in various values of traction ratio below the locked zone between different slow-slip cycles (Fig. S4). Accelerating SSE fronts, as in our 2014 SSE model, have been observed before the 2014 Chile earthquake[21] and before larger earthquakes in Japan[46], which was suggested as a potential precursory signal indicating megathrust earthquake nucleation.

In contrast, traction ratios increase considerably less during the earlier three modeled SSEs (blue lines in Fig. 3 and Fig. S3). Shear stresses temporally increase during the 2002 and 2006 SSEs but decrease during the 2009-2010 event. For example, the peak traction ratio in the 2014 episode is about 3.23% higher than in the preceding 2009-2010 event, corresponding to a 0.1 MPa increase in shear stress. We highlight that the long-term increase of the peak traction ratio at the hypocentral depth during the 20-year-long simulation is small compared to the transient traction changes during the 2014 SSE (Fig. 3). None of the three earlier events leads to traction ratios large enough to overcome the (prescribed) frictional fault strength in the seismogenic part of the slab in our preferred dynamic rupture model.

Earthquake initiation and dynamics accounting for slow-slip transient stresses

We present the first 3D dynamic rupture models of the 2014 M_w 7.3 Guerrero earthquake. Our rupture scenarios are informed by the transient stress of preceding slow slip events and additional predefined frictional heterogeneity on the fault. We focus on a preferred model (Fig. 4) that reproduces the key features of geophysical observations and provides physically self-consistent descriptions of earthquake initiation, dominantly governed by SSE-induced shear stress changes, and its dynamics and arrest, which are predominantly governed by predefined frictional asperities. We discuss alternative rupture scenarios probing sensitivity to initial conditions in the Methods section.

We constrain the initial shear stress, normal stress, and pore fluid pressure before the earthquake using our long-term slow-slip cycle model on the same slab geometry. We extract the SSE model state when the traction ratio, which is associated with the SSE fronts, peaks (Fig. 3) to inform the dynamic rupture simulation. We use a linear slip-weakening friction law[47] to describe the co-seismic fault strength and yielding (see Methods: "Linear slip-weakening friction"). Choosing a small critical slip-weakening distance of d_c=0.05 m, which is at the lower limit of seismological observations[1] and the upper limit of laboratory-inferred estimates[2], allows for spontaneous SSE-initiation at the same time as a sustained large earthquake rupture. We assume a statically strong fault (static friction coefficient $\mu_s = 0.626$) in agreement with the high static frictional strength of rocks[48] but effectively weakened by high pore fluid pressure. This specific choice of μ_s allows us to model realistic co-seismic rupture dynamics and arrest, including realistic levels of slip, rupture speed, and stress drop, as well as spontaneous nucleation at 22 km due to the modeled 2014 SSE event. An alternative, less realistic model with smaller μ_s is shown in Fig S13 and will be discussed in Section 3.

Although earthquake nucleation is linked to the transient stress of the SSE cycle, we show that capturing realistic rupture propagation and arrest requires additional heterogeneity of the megathrust slab. We show that including two circular frictional asperities (see Methods: ”Linear slip-weakening friction”) can reproduce the observed co-seismic characteristics to first-order. We vary the maximum possible frictional strength drop smoothly within each asperity: the dynamic friction coefficient μ_d gradually increases at the edge of the asperities (Methods: “Linear slip-weakening friction”). High variability of dynamic friction has been reported in relation to fault materials and sliding rates in laboratory experiments[49,50] and has been shown to largely affect coseismic rupture dynamics on crustal faults in numerical models[39,51,52].

In our earthquake model, self-sustained dynamic rupture nucleates spontaneously at a depth of 22 km, where the modeled 2014 SSE front acceleration leads to a local increase in shear traction (Fig. 3a,c). This location agrees with the observationally inferred hypocenters within their uncertainties (Fig. 4a-b). Unlike typical dynamic rupture models, where nucleation is prescribed ad hoc [53, e.g.,], spontaneous runaway rupture is here initiated merely by the locally increased shear stress of the preceding SSE transient. Our rupture model dynamically breaks the central asperity and subsequently migrates to the second patch under slightly increasing slip rates (Fig. 4 and Movie S3). The rupture arrests smoothly at the boundaries of the prescribed frictional asperities. The final rupture area is located up-dip from the hypocenter and has no clear overlap with the area that hosts aseismic rupture during slow-slip (Fig S7).

Our preferred earthquake simulation resembles the key observed seismic and geodetic characteristics within observational uncertainties (Fig. 5). Two broad peaks in the moment release rate emerge in our dynamic rupture model, as inferred from teleseismic inversion using more than 70 stations across $35^o - 80^o$ epicentral distance[54] (Fig. 5a). This suggests a multi-asperity rupture process, including dynamic triggering and delays between different asperities (Fig. 5f). In our rupture dynamics model, the first and second peaks appear closer in time than inferred in the inversions which may reflect additional complexities on natural faults and observational uncertainties. For example, the shape of the second asperity area may be varied in our dynamic rupture model to better match the observed moment rate release timing. However, teleseismic inversion lacks the adequate resolution to better inform on the spatial extent of slip[54]. Our modeled total cumulative moment release is $9.41 \times 10^{19} Nm$, which corresponds to a moment magnitude of M_w 7.28 and agrees well with the observations (Fig.5a). An alternative dynamic rupture model with only a single asperity (Methods: ”Model B1”; Fig. S9) fails to reproduce a realistic moment magnitude and the pronounced two-peak character of the moment rate release. Because both dynamic rupture models spontaneously initiate due to the same transient SSE stresses but strongly differ in co-seismic dynamics, we conclude that additional frictional heterogeneity is required to model the propagation dynamics and arrest of the Guerrero earthquake.

Geodetic inversion using permanent on-shore GPS stations yields smaller slip amplitudes[44] but a larger rupture area extending up to the trench, compared to teleseismic inversion[54] (Figs. 5c-d). Similarly, our modeled dynamic rupture features shallow fault slip up-dip of the hypocenter, while our maximum slip amplitude is 2.5 m (Fig. 5e), which is consistent with teleseismic inversion assuming $V_r = 2.5$ km/s[54]. We note that the differences in geodetic and teleseismic fault slip inversions are likely affected by limitations in data resolution and differences in the assumed source time functions, velocity models, and/or fault geometries. Fig. 5b shows the modeled static surface deformation at 80 s after the rupture initiation and its comparison with geodetic observations[33]. There are only two GPS stations (ZIHP and PAPA) with clear recorded signals close to the rupture area and one station (TCPN) with a smaller-amplitude signal distant from the epicenter. Our synthetic surface displacements at ZIHP and PAPA are consistent with the reverse plate movement direction but slightly higher in amplitude than those observed.

Our preferred two-asperity dynamic rupture model reproduces both seismic and geodetic characteristics and is consistent with the localized slip heterogeneity inferred from seismic imaging using regional networks[31,32]. Given the sparsity of co-seismic seismic and geodetic observations, we judge our forward model as data-justified first-order illumination of rupture dynamics and arrest. We note that future incorporation of a high-resolution regional velocity model may improve the achieved observational match.

We analyze the stress drop and energy budget of our preferred dynamic rupture model accounting for the preceding slow-slip cycle with respect to event-specific and global observations. We calculate the average co-seismic stress drop in two different ways: 1) by spatially averaging the on-fault stress drop, and 2) by averaging the modeled stress drop based on energy considerations[55,56] (see Methods: ”Fracture energy and stress drop”). The two approaches result in average model stress drops of 1.74 MPa and 2.1 MPa, respectively. These values are within the expected uncertainties[57] of the seismological inference of 2.94 MPa[54] and are consistent with the global average of the inferred megathrust earthquake stress drops[58].

Next, we analyze the earthquake initiation energy budgets accounting for the transient stress shadowed by the preceding SSE. We calculate the average fracture energy across the effective nucleation area directly induced by our modeled 2014 SSE in the hypocentral area as 0.17 MJ/m^2 (see Methods:"Fracture energy and stress drop"). This inference is comparable to the range of nucleation energies (0.1-1 MJ/m^2) estimated for most $M > 8$ Nankai earthquakes in southwestern Japan[59], implying that the transient stresses of aseismic slip may play a ubiquitous role in the nucleation of megathrust earthquakes. In comparison, the dynamic rupture fracture energy averaged across the entire co-seismically slipping fault is only 0.11 MJ/m^2. This is about 35% lower than the SSE fracture energy at the hypocenter governing the nucleation stage and similar to a seismologically inferred global average of 0.1-10 MJ/m^2[58], but 45% lower than the range of 0.2-2.0 MJ/m^2 measured on natural crustal faults[60]. This relatively low overall fracture energy is consistent with the low average stress drop, which results from the assumed elevated pore fluid pressure constrained by regional seismic imaging[31]. The elevated pore fluid pressure at depth is crucial for recovering faulting dynamics during both the long-term SSE and short-term initiation of our dynamic rupture model.

3 Discussion

Our dynamic rupture models of the M_w7.3 Guerrero earthquake initiated by quasi-dynamic models of the preceding long-term SSE cycles illustrate the interaction between aseismic and co-seismic fault slip. It has been suggested that slow slip at the down-dip end of the seismogenic zone transfers shear stresses up-dip[61] or temporally aid up-dip pore fluid migration[30], both of which potentially destabilize the locked portion of the megathrust. We find that the transient increase in the shear-to-effective-normal-stress ratio resulting from the accelerating migration of the preceding slow-slip events can lead to the spontaneous initiation of realistic earthquake rupture and that this process is sensitive to the dynamics of the long-term transient SSE cycle. In our model, the increasing transient shear stress is sufficiently high for spontaneous dynamic rupture without additional weakening mechanisms, such as the effects of thermal pressurization[62]. However, accounting for additional co-seismic weakening may further aid the slow-slip transient initiation of dynamic rupture[63] inherently capturing our here prescribed variability of co-seismic frictional strength drop[56]. Similarly, a recent conceptual model combining shallow SSEs and two asperities finds that the time-dependent balance between stress and strength is complex and not all SSEs directly lead to the nucleation of an earthquake[64], even when no geometrical complexity or pore fluid variation is considered.

Accounting for megathrust asperities in our co-seismic dynamic rupture model is important for reproducing observationally inferred first-order source characteristics. Megathrust asperities have been related to depth-varying seismic and aseismic faulting behaviors[13,65]. While we here parameterize both asperities as dynamically weak (low μ_d), heterogeneity in the initial stresses, structure, effective static fault strength, or pore fluid pressure[10,66] may serve as dynamically viable asperities[37,39,51,67] and additional observations are required to distinguish between them. We show that local shear-stress asperities can lead to equivalent rupture dynamics in Fig. S12 (Methods: "Model A2"). Our parameterization of frictional asperities is relatively simple but effective in reproducing first-order characteristics within the uncertainties of sparsely observed earthquake kinematics. Denser regional seismic and geodetic instrumentation along the central Mexican coast and off-shore, allowing for better imaging of coseismic fault slip, would be crucial to inform and validate data-integrated and physics-based modeling. Our choice of frictional parameters in the dynamic rupture model allows for balancing the depth-dependent fault strength, heterogeneous initial shear stresses, and heterogeneous frictional strength drop to achieve realistic levels of coseismic slip and moment release across a relatively small rupture area in dynamic rupture simulations. This sensitivity is exemplified in Fig.S13a where a slightly lower μ_s results in delayed rupture arrest, a larger rupture area, and over-prediction of the amplitude and arrival of the first peak in the modeled moment release. Although simpler than the rate-and-state friction law used in the long-term SSE cycle simulations, we yield a similar range in reference friction coefficients (Fig. S13b) and comparable behavior in coseismic slip.

Our modeled SSE and coseismic fault slip are located largely off-shore in central Mexico, where a dense array of ocean bottom seismometers (OBS) has discovered episodic shallow tremors, suggesting small-scale slow-slip events or low-frequency earthquakes[32] potentially linked to small asperities up-dip of the slow-slip region. Accounting for additional small-scale heterogeneity on the fault may help explain high-resolution observations, such as complexity in moment release rate and strong ground motions[68] Here, we focus on the one-way interaction between the SSE cycle and dynamic rupture and omit the respective influence of coseismic rupture on slow-slip transients. Modeling 3D fully dynamic earthquake cycles on geometrically complex faults[69–71] that incorporate spontaneous (aseismic) nucleation, dynamic rupture, and post-seismic deformation are computationally challenging but are becoming achievable at realistic scales and levels of complexity to allow for direct observational verification. Extending our approach to a unified and fully coupled slow-slip and dynamic rupture framework is a promising future step.

Conclusions

Our mechanically self-consistent and data-driven 3D models of long-term SSE cycles, megathrust earthquake initiation, and rupture dynamics in the Guerrero Seismic Gap contribute to a better understanding of the earthquake generation process and can potentially lead to improved time-dependent operational earthquake forecasting[72]. By incorporating the transient stress evolution of slow-slip before coseismic rupture and asperities in co-seismic friction drop, our models reproduce the kinematic and dynamic characteristics of both aseismic slip and coseismic rupture and reveal their physical link. Although long-term stress does not continuously accumulate, the accelerating migrating SSE fronts transiently increase shear stress at the down-dip end of the seismogenic portion of the megathrust. Improvements in the detection of transient aseismic slip deformation will aid in assessing seismic hazards in coastal regions[20,73]. Furthermore, identifying distinct acceleration signals might be routinely possible in future regionally dense networks, specifically off-shore[74].

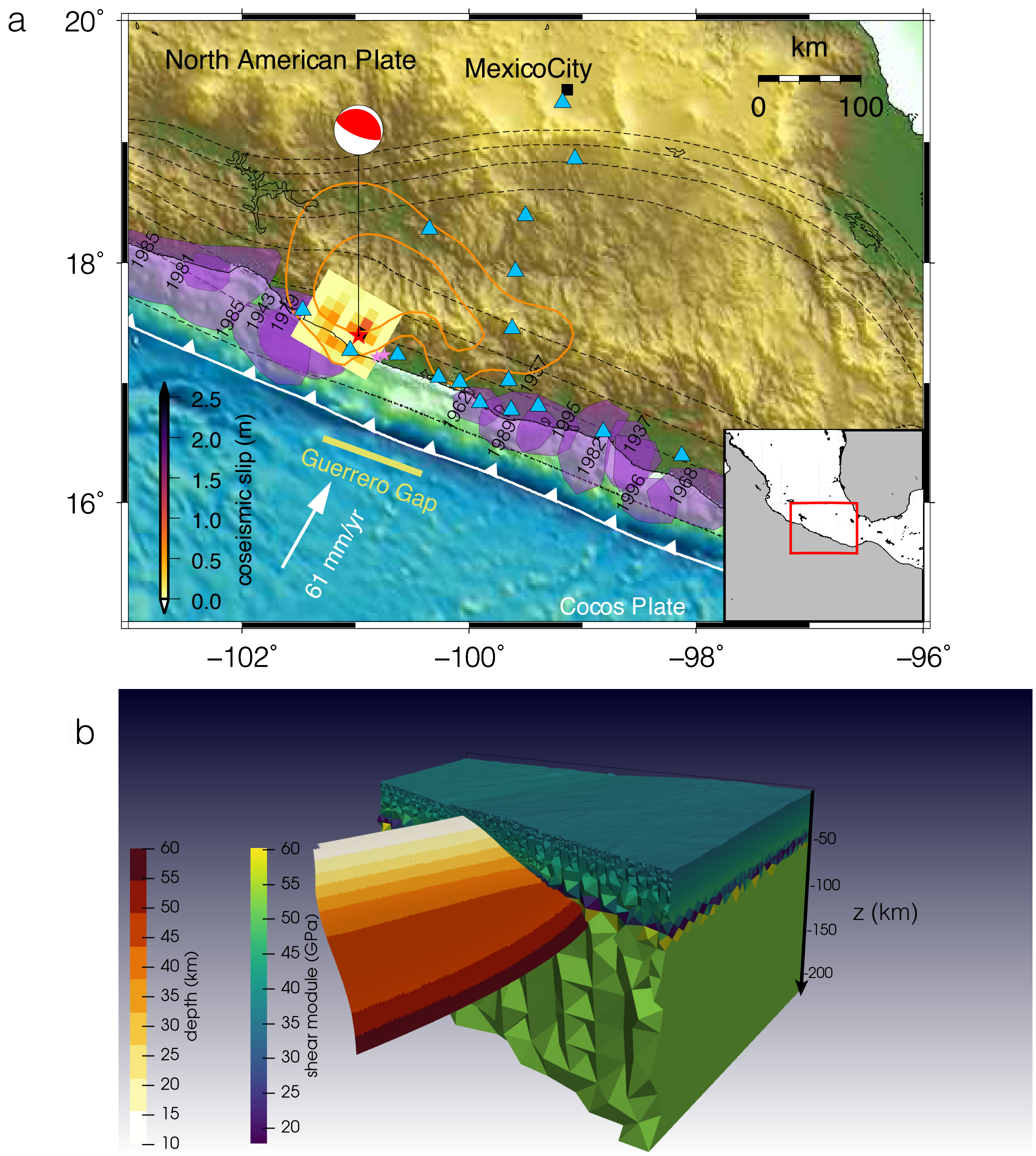

Figure 1. (a) Map of central Mexico where the Cocos plate subducts beneath the North American plate at a rate of 61 mm/yr (PVEL model[75]). The so-called Guerrero Seismic Gap is a 100-km long segment between 100.2^{o}W and 101.2^{o}W (yellow bar) that lacks recent large earthquakes[76]. Purple shades indicate large ($M_\mathrm{w} \leq 6.8$) earthquakes after 1940[76]. The focal mechanism of the 2014 M_w 7.3 Guerrero earthquake is shown in red (strike:304°, dip:21°, rake:99°, Global Centroid Moment Tensor catalog (GCMT)[77,78]). A finite coseismic source model using teleseismic inversion is shown as yellow-to-red-to-black rectangles[54]. The orange contours indicate the 10 cm and 20 cm aseismic levels of fault slip during the 2014 M_w 7.3 slow-slip events[27]. The blue triangles mark the permanent GPS stations used in a geodetic inversion of both the coseismic and slow slip[44]. Depth contours from 5 km depth (trench) to 80 km depth are shown as dashed lines with 5 km depth spacing. Mexico City is shown in black. (b) Slab surface geometry extending from the trench to a depth of 60 km in both slow-slip cycle and dynamic rupture simulations. Tetrahedral elements are color-coded by a 1D layered velocity model from seismic imaging[79] that is used in the dynamic rupture model.

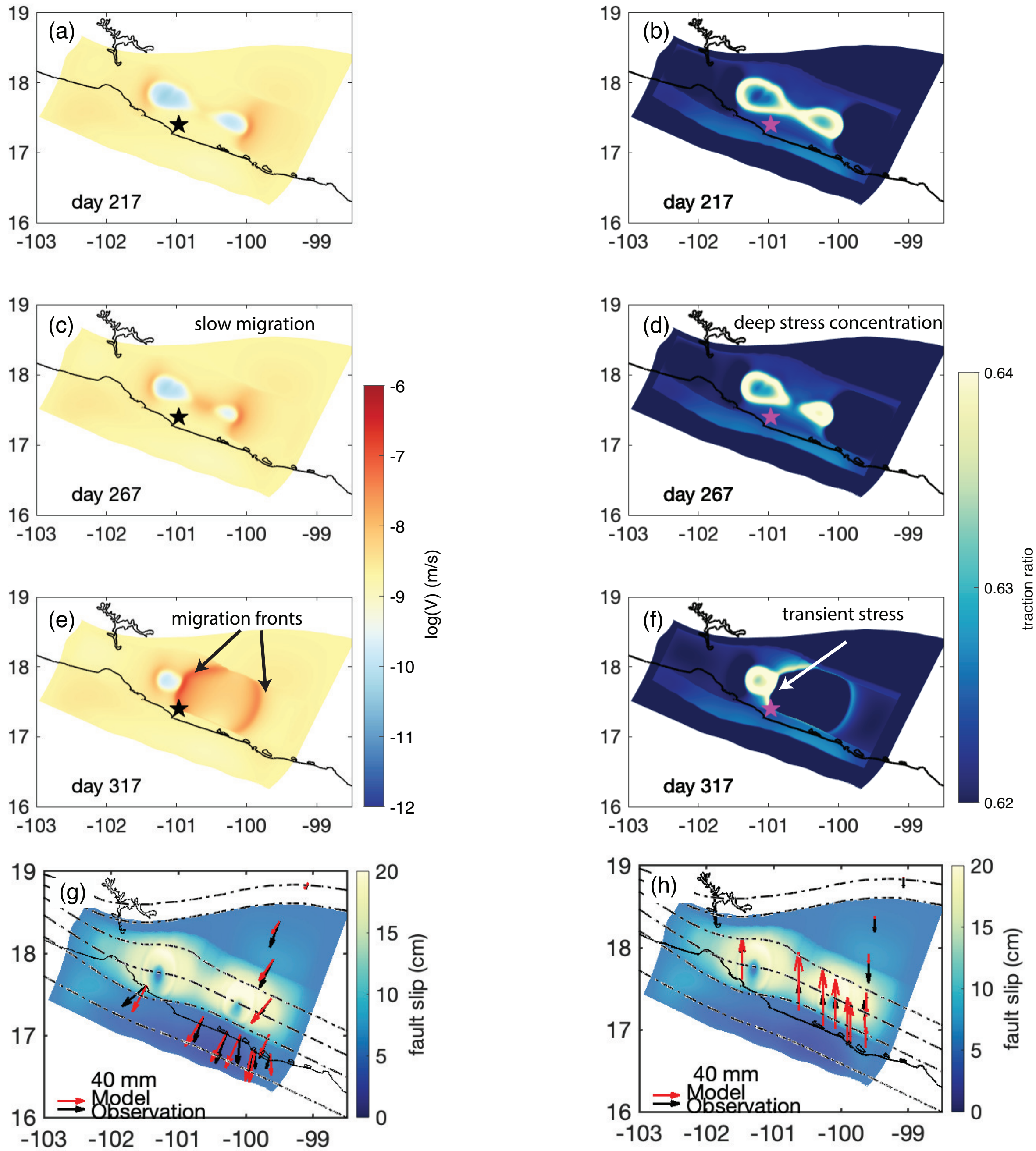

Figure 2. The 2014 SSE in the Guerrero Gap from the preferred quasi-dynamic slow-slip cycle model. Snapshots of fault slip rate (a,c,e) and traction ratios (b,d,f), defined as shear over effective normal stress, on days 217, 267, and 317, respectively. The black star marks the epicenter of the 2014 M_w 7.3 Guerrero earthquake from National Earthquake Information Catalog (USGS NIEC) (https://earthquake.usgs.gov/earthquakes/eventpage/usb000pq41/executive). Slow-slip fault slip rates can reach up to 10^{-6} m/s, which is 1000 times faster than the plate convergence rate (V_{pl} =61 mm/yr). The time-dependent evolution of the fault slip rate is shown in Movie S1 (Supplementary Information). (g), (h): Modeled accumulated 2014 SSE fault slip distribution and surface GPS displacement.The black and red arrows show the observed[33] and synthetic surface GPS displacements, respectively. Dashed black lines are the depth contours of the subducting slab from 20 km to 80 km depth with 20 km depth spacing.

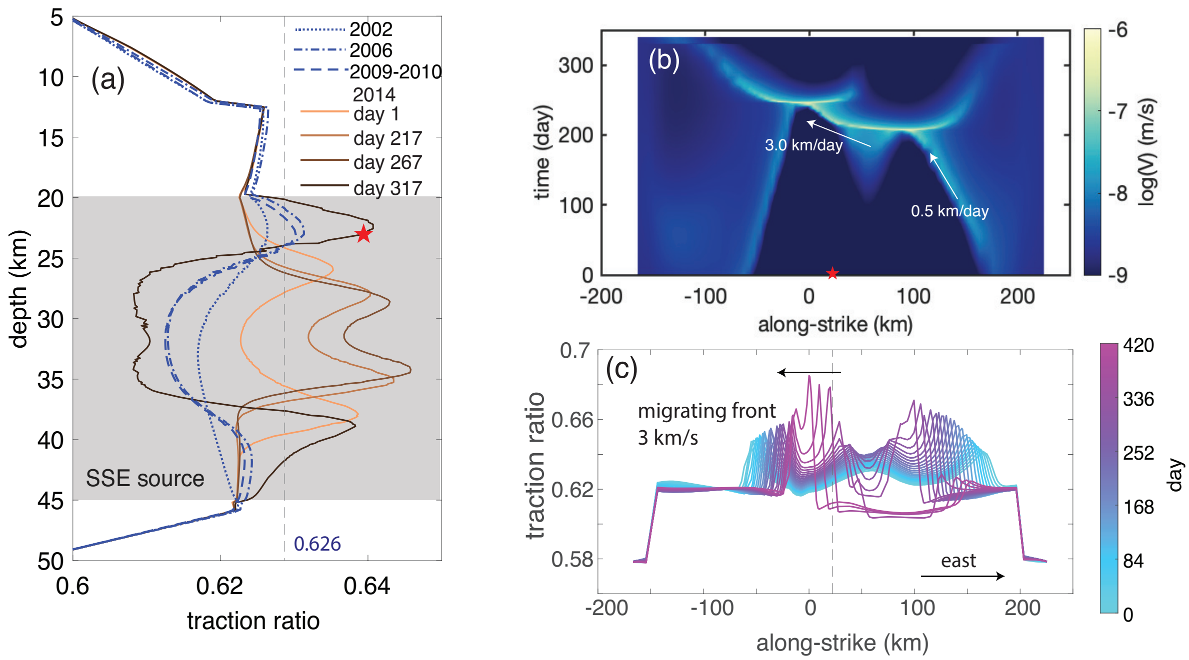

Figure 3. Time-dependent evolution of the on-fault shear-to-effective-normal traction ratio and along-strike migration speed during the modeled SSE cycle. The red star marks the USGS catalog hypocenter of the 2014 M_w7.3 Guerrero earthquake. (a) Cross-sections of the traction ratio during the four modeled subsequent SSEs. Colored solid lines indicate the traction ratios on days 1, 217, 267, and 317 of the modeled 2014 SSE. The blue dot-dashed and dot-dashed lines represent the traction ratios of the three SSE episodes in 2002, 2006, and 2009-2010, respectively. The dashed gray line indicates the static friction coefficient on-fault ($\mu_s = 0.626$) assumed in the dynamic rupture earthquake simulation. (b) Spatial and temporal evolution of the on-fault slow-slip rate along the 20 km depth contour. The white vectors indicate the averaged migrating speeds of the slip front at y=150 km and y=0 km. (c) Profiles of the traction ratio sampled every 10 days along the 30 km depth contour during the modeled SSE cycle illustrate the westward acceleration of the SSE migration front.

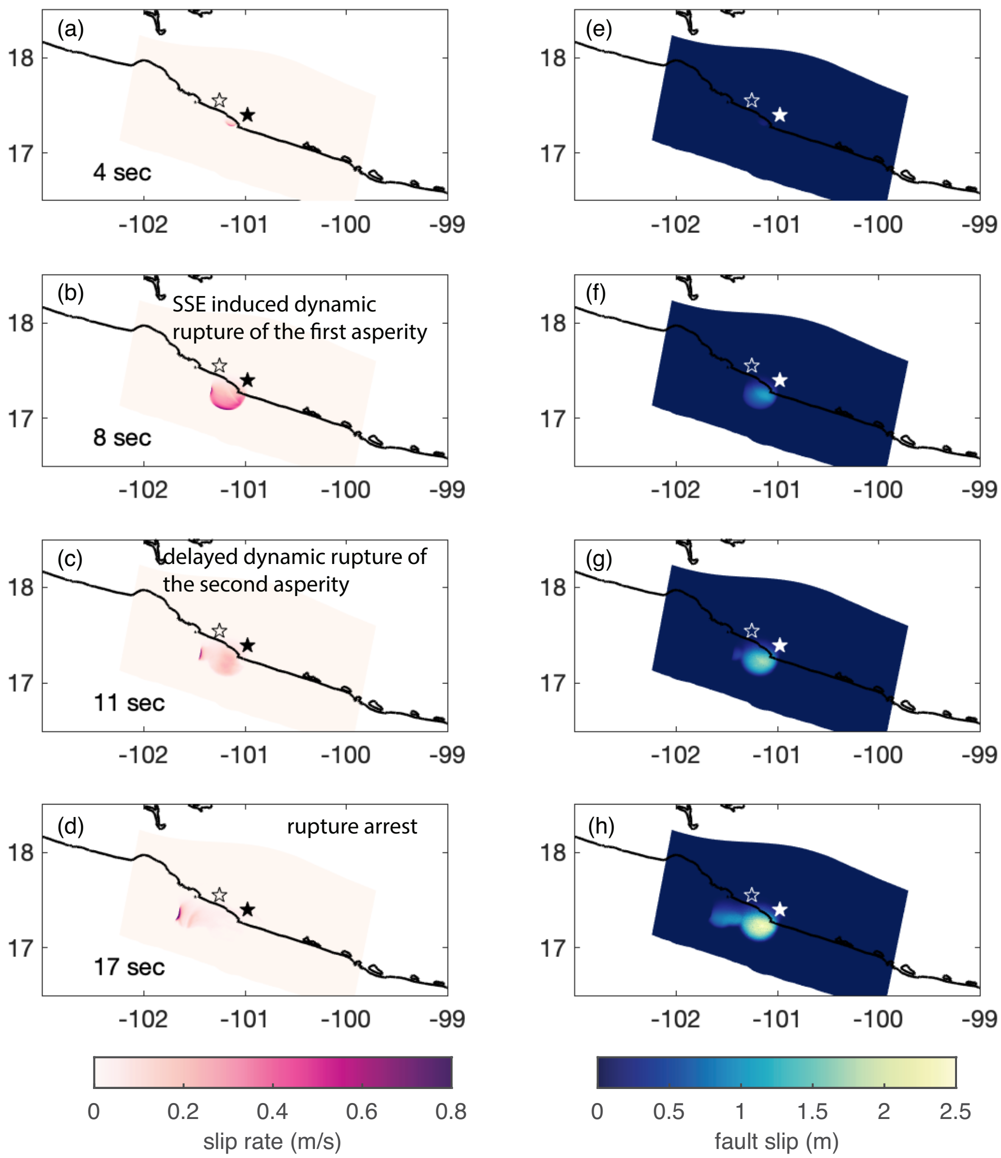

Figure 4. Preferred dynamic rupture model of the 2014 M_w 7.3 Guerrero earthquake. Snapshots of the modeled coseismic fault slip rate (left panels) and fault slip (right panels) at 4 s, 8 s, 11 s, and 17 s, respectively. (a): spontaneous nucleation governed by shear stress transients of the long-term SSE cycle, (b): SSE initiated dynamic rupture of the first asperity, (c): delayed rupture of the second asperity, and (d): the dynamic arrest of rupture (Supplementary Movie S3). The corresponding fault slip at each time step is shown in (e)-(h), respectively. The coastline is indicated by the black line. Solid and empty stars indicate the different hypocenter locations from the USGS and GCMT catalogs, respectively.

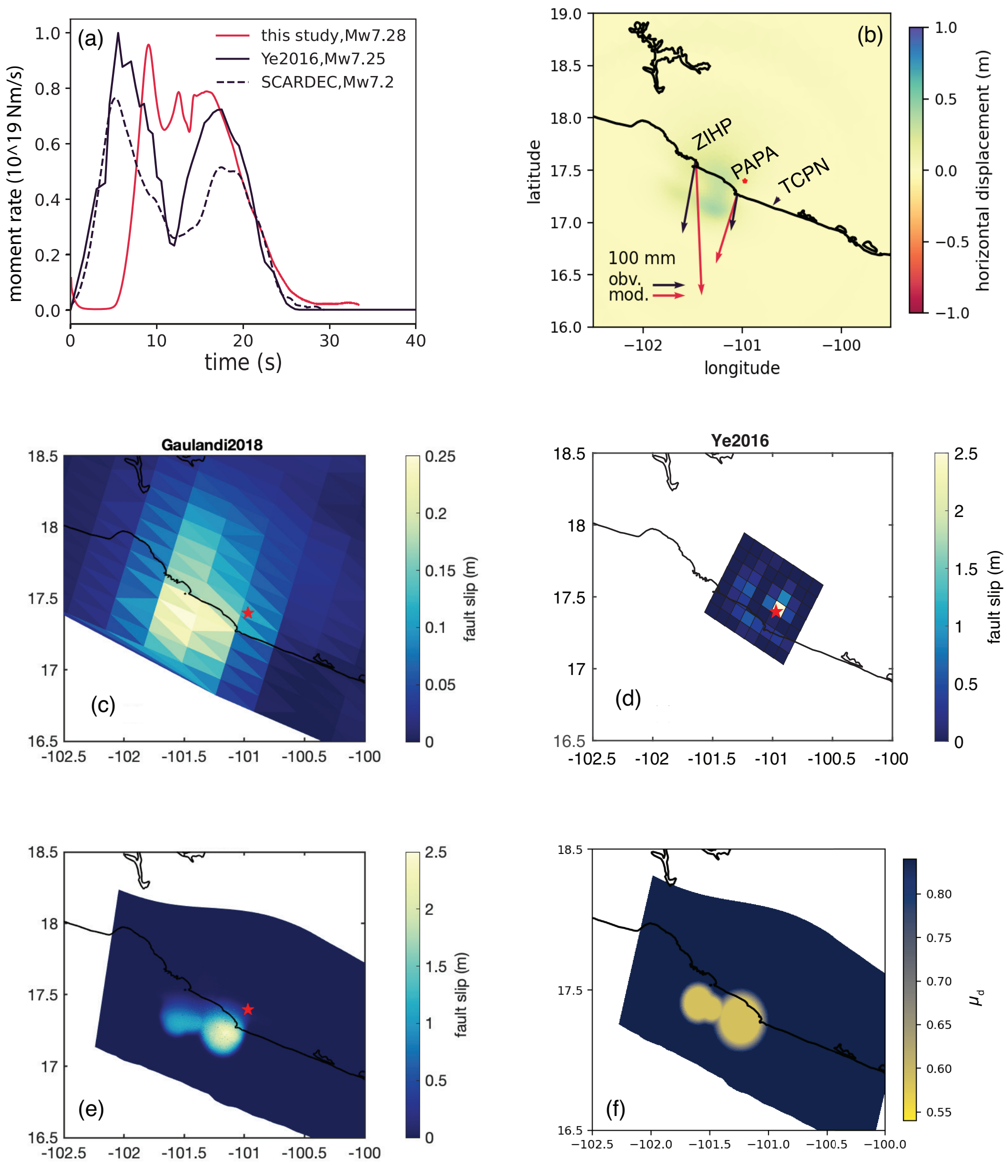

Figure 5. Observational verification of kinematic and dynamic source characteristics of the dynamic rupture model of the 2014 M_w7.3 Guerrero earthquake. (a) On-fault dynamic rupture moment rate compared to teleseismic inversion[54] and SCARDEC (http://scardec.projects.sismo.ipgp.fr)[80]. (b) Mapview with horizontal surface displacements observed at continuous GPS stations (black[33]) and in our simulation (red). The red star marks the USGS catalog hypocenter. Accumulated fault slip from (c) regional geodetic inversion[33], (d) teleseismic inversion[54], and (e) preferred dynamic rupture scenario. The maximum slip is 0.25 m, 2.5 m and 2.5 m, respectively. (f) Distribution of the prescribed heterogeneous dynamic friction coefficient μ_d which gradually increases from 0.546 within to 0.826 at the edge of the asperities following an exponential function (see Methods: "Linear slip-weakening friction").

References

1. Dragert, H., Wang, K. & James, T. S. A silent slip event on the deeper Cascadia subduction interface. *Science* **292**, 1525–1528, DOI: 10.1126/science.1060152 (2001).

2. Shelly, D. R., Beroza, G. C., Ide, S. & Nakamula, S. Low-frequency earthquakes in Shikoku, Japan, and their relationship to episodic tremor and slip. *Nature* **442**, 188–191, DOI: 10.1038/nature04931 (2006).

3. Douglas, A., Beavan, J., Wallace, L. & Townend, J. Slow slip on the northern Hikurangi subduction interface, New Zealand. *Geophys. Res. Lett.* **32**, DOI: 10.1029/2005GL023607 (2005).

4. Schwartz, S. Y. & Rokosky, J. M. Slow slip events and seismic tremor at circum-Pacific subduction zones. *Rev. Geophys.* **45**, DOI: 10.1029/2006RG000208. (2007).

5. Peng, Z. & Gomberg, J. An integrated perspective of the continuum between earthquakes and slow-slip phenomena. *Nat. Geosci.* **3**, 599–607, DOI: 10.1038/ngeo940 (2010).

6. Linde, A. T., Gladwin, M. T., Johnston, M. J., Gwyther, R. L. & Bilham, R. G. A slow earthquake sequence on the san andreas fault. *Nature* **383**, 65 (1996).

7. Rousset, B., Bürgmann, R. & Campillo, M. Slow slip events in the roots of the san andreas fault. *Sci. Adv.* **5**, eaav3274, DOI: 10.1126/sciadv.aav3274 (2019).

8. Shelly, D. R., Beroza, G. C. & Ide, S. Non-volcanic tremor and low-frequency earthquake swarms. *Nature* DOI: 10.1038/nature05666 (2007).

9. Khoshmanesh, M., Shirzaei, M. & Uchida, N. Deep slow-slip events promote seismicity in northeastern japan megathrust. *Earth Planet. Sci. Lett.* **540**, DOI: 10.1016/j.epsl.2020.116261 (2020).

10. Bürgmann, R. The geophysics, geology and mechanics of slow fault slip. *Earth Planet. Sci. Lett.* **495**, 112–134, DOI: https://doi.org/10.1016/j.epsl.2018.04.062 (2018).

11. Tobin, H. J. & Saffer, D. M. Elevated fluid pressure and extreme mechanical weakness of a plate boundary thrust, nankai trough subduction zone. *Geology* **37**, 679–682 (2009).

12. Wang, K. Finding fault in fault zones. *Science* **329**, 152–153, DOI: 10.1126/science.1192223 (2010).

13. Lay, T. *et al.* Depth-varying rupture properties of subduction zone megathrust faults. *J. Geophys. Res.* **117**, B04311, DOI: https://doi.org/10.1029/2011JB009133 (2012).

14. Li, D. & Liu, Y. Spatiotemporal evolution of slow slip events in a non-planar fault model for northern cascadia subduction zone. *J. Geophys. Res. Solid Earth* **63**, 959–968, DOI: 10.1002/2016JB012857 (2016).

15. Ulrich, T., Gabriel, A.-A. & Madden, E. H. Stress, rigidity and sediment strength control megathrust earthquake and tsunami dynamics. *Nat. Geosci.* **15**, 67–73, DOI: 10.1038/s41561-021-00863-5 (2022).

16. Gao, X. & Wang, K. Rheological separation of the megathrust seismogenic zone and episodic tremor and slip. *Nature* (2017).

17. Saffer, D. M. & Wallace, L. M. The frictional, hydrologic, metamorphic and thermal habitat of shallow slow earthquakes. *Nat. Geosci.* **8**, 594–600, DOI: 10.1038/ngeo2490 (2015).

18. Frank, W. B. *et al.* Uncovering the geodetic signature of silent slip through repeating earthquakes. *Geophys. Res. Lett.* 2774–2779, DOI: 10.1002/2015gl063685 (2015).

19. Zhu, W., Allison, K. L., Dunham, E. M. & Yang, Y. Fault valving and pore pressure evolution in simulations of earthquake sequences and aseismic slip. *Nat. communications* **11**, 4833, DOI: 10.1038/s41467-020-18598-z (2020).

20. Kato, A. *et al.* Propagation of slow slip leading up to the 2011 mw 9.0 tohoku-oki earthquake. *Science* **335**, 705–708, DOI: 10.1126/science.1215141 (2012).

21. Socquet, A. *et al.* An 8 month slow slip event triggers progressive nucleation of the 2014 chile megathrust. *Geophys. Res. Lett.* **44**, 4046–4053, DOI: 10.1002/2017gl073023 (2017).

22. Ruiz, S. *et al.* Intense foreshocks and a slow slip event preceded the 2014 iquique mw8.1 earthquake. *Science* **345**, 1165–1169, DOI: 10.1126/science.1256074 (2014).

23. Obara, K. & Kato, A. Connecting slow earthquakes to huge earthquakes. *Science* **353**, 253–257 (2016).

24. Pritchard, M. E. *et al.* New opportunities to study earthquake precursors. *Seism. Res. Lett.* **91**, 2444–2447, DOI: 10.1785/0220200089 (2020).

25. Kostoglodov, V., Bandy, W., Dominguez, J. & Mena, M. Gravity and seismicity over the Guerrero seismic gap, Mexico. *Geophys. Res. Lett* **23**, 3385–3388 (1996).

26. Radiguet, M. *et al.* Slow slip events and strain accumulation in the guerrero gap, mexico. *J. Geophys. Res. Solid Earth* **117**, DOI: 10.1029/2011JB008801 (2012).

27. Radiguet, M. *et al.* Triggering of the 2014 mw7.3 papanoa earthquake by a slow slip event in guerrero, mexico. *Nat. Geosci* DOI: 10.1038/ngeo2817 (2016).

28. Pérez-Campos, X. *et al.* Horizontal subduction and truncation of the cocos plate beneath central mexico. *Geophys. Res. Lett.* **35**, DOI: doi:10.1029/2008GL035127 (2008).

29. Husker, A. L. *et al.* Temporal variations of non-volcanic tremor (nvt) locations in the mexican subduction zone: Finding the nvt sweet spot. *Geochem. Geophys. Geosystems* **13** (2012).

30. Frank, W. *et al.* Along-fault pore-pressure evolution during a slow-slip event in guerrero, mexico. *Earth Planet. Sci. Lett.* **413**, 135–143, DOI: http://dx.doi.org/10.1016/j.epsl.2014.12.051 (2015).

31. Song, T. R. *et al.* Subducting slab ultra-slow velocity layer coincident with silent earthquakes in southern mexico. *Science* **324**, 502–6, DOI: 10.1126/science.1167595 (2009).

32. Plata-Martinez, R. *et al.* Shallow slow earthquakes to decipher future catastrophic earthquakes in the guerrero seismic gap. *Nat. communications* **12**, 3976, DOI: 10.1038/s41467-021-24210-9 (2021).

33. Gualandi, A., Perfettini, H., Radiguet, M., Cotte, N. & Kostoglodov, V. Gps deformation related to the mw 7.3, 2014, papanoa earthquake (mexico) reveals the aseismic behavior of the guerrero seismic gap. *Geophys. Res. Lett.* **44**, 6039–6047 (2017).

34. Oglesby, D. D. & Mai, P. M. Fault geometry, rupture dynamics and ground motion from potential earthquakes on the north anatolian fault under the sea of marmara. *Geophys. J. Int.* **188**, 1071–1087, DOI: https://doi.org/10.1111/j.1365-246X.2011.05289.x (2012).

35. Gabriel, A.-A., Ampuero, J.-P., Dalguer, L. A. & Mai, P. M. The transition of dynamic rupture styles in elastic media under velocity-weakening friction. *J. Geophys. Res.* **117**, DOI: doi:10.1029/2012JB009468 (2012).

36. van Zelst, I., Wollherr, S., Gabriel, A.-A., Madden, E. H. & van Dinther, Y. Modeling megathrust earthquakes across scales: One-way coupling from geodynamics and seismic cycles to dynamic rupture. *J. Geophys. Res. Solid Earth* **124**, 11414–11446, DOI: https://doi.org/10.1029/2019JB017539 (2019).

37. Harris, R. A. *et al.* A geology and geodesy based model of dynamic earthquake rupture on the rodgers creek-hayward-calaveras fault system, california. *J. Geophys. Res. Solid Earth* **126**, DOI: https://doi.org/10.1029/2020JB020577 (2021).

38. Ramos, M. D. *et al.* Assessing margin-wide rupture behaviors along the cascadia megathrust with 3-d dynamic rupture simulations. *J. Geophys. Res.* **126**, e2021JB022005, DOI: https://doi.org/10.1029/2021JB022005 (2021).

39. Tinti, E. *et al.* Constraining families of dynamic models using geological, geodetic and strong ground motion data: The mw 6.5, october 30th, 2016, norcia earthquake, italy. *Earth Planet. Sci. Lett.* **576**, DOI: 10.1016/j.epsl.2021.117237 (2021).

40. He, C., Wang, Z. & Yao, W. Frictional sliding of gabbro gouge under hydrothermal conditions. *Tectonophys.* **445**, 353–362, DOI: 10.1016/j.tecto.2007.09.008 (2007).

41. Manea, V. C. & Manea, M. Flat-slab thermal structure and evolution beneath central mexico. *Pure Appl. Geophys.* **168**, 1475–1487, DOI: 10.1007/s00024-010-0207-9 (2011).

42. Perez-Silva, A., Li, D., Gabriel, A.-A. & Kaneko, Y. 3d modeling of long-term slow slip events along the flat-slab segment in the guerrero seismic gap, mexico. *Geophys. Res. Lett.* **48**, e2021GL092968, DOI: https://doi.org/10.1029/2021GL092968 (2021).

43. Audet, P., Bostock, M. G., Christensen, N. I. & Peacock, S. M. Seismic evidence for overpressured subducted oceanic crust and megathrust fault sealing. *Nature* **457**, 76–78, DOI: 10.1038/nature07650 (2009).

44. Gualandi, A., Perfettini, H., Radiguet, M., Cotte, N. & Kostoglodov, V. Gps deformation related to the mw 7.3, 2014, papanoa earthquake (mexico) reveals the aseismic behavior of the guerrero seismic gap. *Geophys. Res. Lett.* **44**, 6039–6047, DOI: 10.1002/2017gl072913 (2017).

45. Kaneko, Y., Fukuyama, E. & Hamling, I. J. Slip-weakening distance and energy budget inferred from near-fault ground deformation during the 2016 mw7.8 kaikoura earthquake. *Geophys. Res. Lett.* **44**, 4765–4773, DOI: https://doi.org/10.1002/2017GL073681 (2017).

46. Uchida, N., Iinuma, T., Nadeau, R. M., Bürgmann, R. & Hino, R. Periodic slow slip triggers megathrust zone earthquakes in northeastern japan. *Science* **351**, 488–492, DOI: doi:10.1126/science.aad3108 (2016).

47. Andrews. Dynamic plane-strain shear rupture with a slip-weakening friction law calculated by a boundary integral method. *BSSA* DOI: https://doi.org/10.1785/BSSA0750010001 (1985).

48. Byerlee, J. *Friction of rocks*, 615–626 (Springer, 1978).

49. Di Toro, G., Goldsby, D. L. & Tullis, T. E. Friction falls towards zero in quartz rock as slip velocity approaches seismic rates. *Nature* **427**, 436–439, DOI: 10.1038/nature02249 (2004).

50. Collettini, C., Tesei, T., Scuderi, M., Carpenter, B. & Viti, C. Beyond byerlee friction, weak faults and implications for slip behavior. *Earth Planet. Sci. Lett.* **519**, 245–263, DOI: https://doi.org/10.1016/j.epsl.2019.05.011 (2019).

51. Ramos, M. D. & Huang, Y. How the transition region along the cascadia megathrust influences coseismic behavior: Insights from 2-d dynamic rupture simulations. *Geophys. Res. Lett.* **46**, 1973–1983 (2019).

52. Aochi, H. & Twardzik, C. Imaging of seismogenic asperities of the 2016 ml 6.0 amatrice, central italy, earthquake through dynamic rupture simulations. *Pure Appl. Geophys.* **177**, 1931–1946, DOI: 10.1007/s00024-019-02199-z (2020).

53. Galis, M. *et al.* On the initiation of sustained slip-weakening ruptures by localized stresses. *Geophys. J. Int.* **200**, 890–909, DOI: 10.1093/gji/ggu436 (2014).

54. Ye, L., Lay, T., Kanamori, H. & Rivera, L. Rupture characteristics of major and great ($m_w \leq 7.0$) megathrust earthquakes from 1990 to 2015: 2.depth dependence. *J. Geophys. Res.* **121**, 845–863, DOI: 10.1002/2015jb012427 (2016).

55. Noda, H., Lapusta, N. & Kanamori, H. Comparison of average stress drop measures for ruptures with heterogeneous stress change and implications for earthquake physics. *Geophys. J. Int.* **193**, 1691–1712, DOI: 10.1093/gji/ggt074 (2013).

56. Perry, S. M., Lambert, V. & Lapusta, N. Nearly magnitude-invariant stress drops in simulated crack-like earthquake sequences on rate-and-state faults with thermal pressurization of pore fluids. *J. Geophys. Res.* **125**, e2019JB018597, DOI: https://doi.org/10.1029/2019JB018597 (2020).

57. Abercrombie, R. E. Resolution and uncertainties in estimates of earthquake stress drop and energy release. *Philos. Transactions Royal Soc. A: Math. Phys. Eng. Sci.* **379**, 20200131, DOI: doi:10.1098/rsta.2020.0131 (2021).

58. Abercrombie, R. E. & Rice, J. R. Can observations of earthquake scaling constrain slip weakening? *Geophys. J. Int.* **162**, 406–424 (2005).

59. Kato, N. Fracture energies at the rupture nucleation points of large interplate earthquakes. *Earth Planet. Sci. Lett.* **353-354**, 190–197, DOI: https://doi.org/10.1016/j.epsl.2012.08.015 (2012).

60. Tinti, E., Spudich, P. & Cocco, M. Earthquake fracture energy inferred from kinematic rupture models on extended faults. *J. Geophys. Res.* **110**, DOI: 10.1029/2005jb003644 (2005).

61. Liu, Y. & Rice, J. R. Spontaneous and triggered aseismic deformation transients in a subduction fault model. *J. Geophys. Res.* **112**, DOI: 10.1029/2007JB004930 (2007).

62. Noda, H., Dunham, E. M. & Rice, J. R. Earthquake ruptures with thermal weakening and the operation of major faults at low overall stress levels. *J. Geophys. Res.* **114**, DOI: 10.1029/2008JB006143 (2009).

63. Hirono, T. *et al.* Near-trench slip potential of megaquakes evaluated from fault properties and conditions. *Sci. reports* **6**, 28184, DOI: 10.1038/srep28184 (2016).

64. Meng, Q. & Duan, B. Dynamic modeling of interactions between shallow slow-slip events and subduction earthquakes. *Seism. Res. Lett.* DOI: 10.1785/0220220138 (2022).

65. Walton, M. A. *et al.* Toward an integrative geological and geophysical view of cascadia subduction zone earthquakes. *Annu. Rev. Earth Planet. Sci.* **49**, 367–398, DOI: 10.1146/annurev-earth-071620-065605 (2021).

66. Bilek, S. L. & Lay, T. Rigidity variations with depth along interplate megathrust faults in subduction zones. *Nature* **400**, 443–446, DOI: 10.1038/22739 (1999).

67. Madden, E. H., Ulrich, T. & Gabriel, A.-A. The state of pore fluid pressure and 3-d megathrust earthquake dynamics. *J. Geophys. Res.* **127**, e2021JB023382, DOI: https://doi.org/10.1029/2021JB023382 (2022).

68. Galvez, P., Dalguer, L. A., Ampuero, J. & Giardini, D. Rupture reactivation during the 2011 mw 9.0 tohoku earthquake: Dynamic rupture and ground-motion simulationsrupture reactivation during the 2011 mw 9.0 tohoku earthquake: Dynamic rupture and ground-motion simulations. *Bull. Seism. Soc. Am.* **106**, 819–831, DOI: 10.1785/0120150153 (2016).

69. Jiang, J. *et al.* Community-driven code comparisons for three-dimensional dynamic modeling of sequences of earthquakes and aseismic slip. *J. Geophys. Res.* **127**, e2021JB023519, DOI: https://doi.org/10.1029/2021JB023519 (2022).

70. Erickson, B. A. *et al.* Incorporating full elastodynamic effects and dipping fault geometries in community code verification exercises for simulations of earthquake sequences and aseismic slip (seas). *Bull. Seism. Soc. Am.* DOI: 10.1785/0120220066 (2023).

71. Uphoff, C., May, D. A. & Gabriel, A.-A. A discontinuous galerkin method for sequences of earthquakes and aseismic slip on multiple faults using unstructured curvilinear grids. *Geophys. J. Int.* **233**, 586–626 (2023).

72. Uchida, N. & Bürgmann, R. A decade of lessons learned from the 2011 tohoku-oki earthquake. *Rev. Geophys.* **59**, DOI: https://doi.org/10.1029/2020RG000713 (2021).

73. Socquet, A. *et al.* An 8 month slow slip event triggers progressive nucleation of the 2014 chile megathrust. *Geophys. Res. Lett.* **44**, 4046–4053, DOI: 10.1002/2017gl073023 (2017).

74. Hilley, G. E. *et al.* Sz4d implementation plan. *SZ4D* DOI: https://doi.org/10.25740/hy589fc7561 (2022).

75. DeMets, C., Gordon, R. G. & Argus, D. F. Geologically current plate motions. *Geophys. J. Int.* **181**, 1–80, DOI: 10.1111/j.1365-246X.2009.04491.x (2010).

76. Lowry, A. R., Larson, K. M., Kostoglodov, V. & Bilham, R. Transient fault slip in Guerrero, southern Mexico. *Geophys. Res. Lett.* **28**, 3753–3756 (2001).

77. Dziewonski, A. M., Chou, T.-A. & Woodhouse, J. H. Determination of earthquake source parameters from waveform data for studies of global and regional seismicity. *J. Geophys. Res. Solid Earth* **86**, 2825–2852, DOI: https://doi.org/10.1029/JB086iB04p02825 (1981).

78. Ekström, G., Nettles, M. & Dziewoński, A. The global cmt project 2004–2010: Centroid-moment tensors for 13,017 earthquakes. *Phys. Earth Planet. Interiors* **200**, 1–9 (2012).

79. Dougherty, S. L. & Clayton, R. W. Seismicity and structure in central mexico: Evidence for a possible slab tear in the south cocos plate. *J. Geophys. Res.* **119**, 3424–3447, DOI: 10.1002/2013jb010883 (2014).

80. Vallee, M., Charléty, J., Ferreira, A. M. G., Delouis, B. & Vergoz, J. Scardec: a new technique for the rapid determination of seismic moment magnitude, focal mechanism and source time functions for large earthquakes using body-wave deconvolution. *Geophys. J. Int.* **184**, 338–358, DOI: 10.1111/j.1365-246X.2010.04836.x (2011).

81. Audet, P. & Burgmann, R. Possible control of subduction zone slow-earthquake periodicity by silica enrichment. *Nature* **510**, 389–393, DOI: 10.1038/nature13391 (2014).

82. Li, D. & Liu, Y. Modeling slow-slip segmentation in cascadia subduction zone constrained by tremor locations and gravity anomalies. *J. Geophys. Res. Solid Earth* n/a–n/a, DOI: 10.1002/2016JB013778 (2017). 2016JB013778.

83. Day, S. M., Dalguer, L. A., Lapusta, N. & Liu, Y. Comparison of finite difference and boundary integral solutions to three-dimensional spontaneous rupture. *J. Geophys. Res.* **110**, DOI: 10.1029/2005jb003813 (2005).

84. Wollherr, S., Gabriel, A.-A. & Uphoff, C. Off-fault plasticity in three-dimensional dynamic rupture simulations using a modal discontinuous galerkin method on unstructured meshes: implementation, verification and application. *Geophys. J. Int.* **214**, 1556–1584, DOI: 10.1093/gji/ggy213 (2018).

85. Oeser, J., Bunge, H.-P. & Mohr, M. Cluster design in the earth sciences tethys. In *International conference on high performance computing and communications*, 31–40 (Springer, 2006).

bibliographystylenaturemag-doi

4 Methods

3D quasi-dynamic simulations of the long-term slow-slip cycles

Direct observations of slow-slip cycles are limited, motivating numerical simulations to elucidate the underlying mechanics of SSE and earthquake interactions. We simulate long-term slow-slip sequences on a convergent plate boundary and analyze the time-dependent evolution of slip rates and shear stresses on the fault interface in 3D. We use a quasi-dynamic formulation and the Boundary Element Method (BEM). Our forward model adopts a laboratory-derived rate-and-state friction law and a 3D realistic subducting slab geometry beneath central Mexico. The governing equations relate the temporal shear stress evolution of an individual element in response to fault slip and long-term plate convergence following Rice [1993][3] as

$$\tau_i(t) = -\sum_{j=1}^{N} K_{i,j}\left(\delta_j(t) - V_{pl}t\right) - \eta\frac{d\delta_i(t)}{dt}, \tag{1}$$

where $\delta_i(t)$ is the fault slip and $K_{i,j}$ is the shear stress in element j due to a unit dislocation in dip direction of element i. The static Green's function $K_{i,j}$ is calculated using triangular dislocations in a uniform half-space[4] assuming a homogeneous shear modulus of $\mu = 30$ GPa and density $\rho = 2670 kg/m^3$. The plate convergent rate V_{pl} is set to be uniformly 61 mm/year based on a global plate motion model, the PVEL model[75].

We use the open-source code TriBIE (https://github.com/daisy20170101/TriBIE)[14,42], which is parallelized with OpenMPI and has been verified in 2D and 3D community benchmark exercises[69,70]. We here use the quasi-dynamic approach approximating inertia effects with radiation damping for our SSE cycle simulations. To this end, the radiation damping factor $\eta = \mu/(2c_s)$ (with c_s being the shear wave speed) is introduced[3]. Compared to fully dynamic simulations, the quasi-dynamic approach can lead to similar overall seismic cycle behavior but differing rupture dynamics[8,9,69]. We detail all slow-slip cycle modeling parameters in the following.

Effective normal stress

Figure S1d shows the along-depth profiles of our assumed effective normal stress $\bar{\sigma}_n$, pore fluid pressure (p_f), hydrostatic (0.37*σ_z) and lithostatic pressures (σ_z). We assume that lithostatic pressure is depth-dependent with a constant overburden gradient (i.e., $\sigma_z = \rho g(-z)$). The effective normal stress, defined as the difference between lithostatic pressure and pore fluid pressure, increases with depth at a constant gradient $\bar{\sigma}_n = 28MPa/km$ until a depth of 2.7 km. At lower depths, effective normal stress remains constant as $\bar{\sigma}_n = 50$ MPa except at the SSE source depth between 20 and 45 km. Effective normal stress of 50 MPa at seismogenic depth is a common assumption used in community benchmark studies[69].

To reproduce the relatively low stress drops inferred for SSEs, we assume a low effective normal stress of $\bar{\sigma}_n^{SSE} = 2.5$ MPa at depths between 20 km and 45 km based on our previous work for a narrower slab geometry[42] and linked to elevated pore fluid pressure. Such high, near-lithostastic pore fluid pressure is supported by the observed elevated ratio between V_p and V_s from seismic imaging along the coast of southwest Japan, Cascadia, and central Mexico[31,81].

Rate-and-state friction

Fault shear strength in the quasi-dynamic SSE simulation is governed by a laboratory-derived rate and state-dependent friction law, the aging law[10,11]. The effective friction coefficient f depends on the fault slip rate v and a single state variable θ as

$$\tau = \bar{\sigma}_n f = (\sigma_n - p)\left[f_0 + a\ln\left(\frac{v}{v_0}\right) + b\ln\left(\frac{v_0\theta}{D_{RS}}\right)\right]. \tag{2}$$

Here, a and b are non-dimensional friction parameters for the direct effect and evolution effect, respectively, D_{RS} is the characteristic slip distance over which θ evolves in response to velocity steps, f_0 is the friction coefficient at a reference velocity v_0 at steady state, and $\bar{\sigma}_n = \sigma_n - p_f$ is the effective normal stress, defined as lithostatic loading stress minus the pore fluid pressure.

At steady state $\theta = D_{RS}/v$, the friction coefficient is $f_{ss} = f_0 + (a-b)\ln(\frac{v}{v_0})$. Slip remains stable, and any slip perturbation evolves toward a steady state when the friction stability parameter $(a-b)$ is positive (velocity-strengthening, VS). Slip can be either unstable or conditionally stable when $(a-b)$ is negative (velocity-weakening, VW). We use uniform distributions for the initial slip rate V_{ini} and the initial state variable θ_{ini} on the entire fault.

We adopt the definition of the critical nucleation length h^*_{RA} based on the fracture energy balance for a quasi-statically expanding crack[12],

$$h^*_{RA} = \frac{2\mu b D_{RS}}{\pi(1-\nu)(b-a)^2\bar{\sigma}}. \tag{3}$$

Here, we assume a shear modulus of $\mu = 30$ GPa and Poisson's ratio of $\nu = 0.25$. The ratio between the maximum width of the velocity-weakening portion of the slab and the critical nucleation length (h^*_{RA}) significantly affects the slip behavior of modeled SSEs[8,1342,82].

For faults governed by rate-and-state friction, the quasi-static process zone at a non-zero rupture speed can be estimated as $\Lambda_0 = C\frac{\mu^* D_{RS}}{b\sigma_n}$, where C is a constant of order 1[8,69,83], $\mu^* = \mu$ for antiplane strain and $\mu^* = \mu/(1-\nu)$ for plane strain, where ν is Poisson's ratio. We note that our mesh size is considerably smaller than Λ_0 which ensures numerical stability and accuracy.

We adopt the empirical "aging" law that can be interpreted to account for time-dependent healing of microscopic stationary frictional contacts [15, e.g.,], for describing the temporal evolution of state variable (θ):

$$\frac{d\theta}{dt} = 1 - \frac{V\theta}{D_{RS}}. \tag{4}$$

To regularize the solution at low slip rates we use the modification proposed by Rice[16]:

$$\mu = asinh^{-1}[\frac{V}{2v_0}exp(\frac{\mu_0 + b\ln(v_0\theta/D_{RS})}{a})], \tag{5}$$

which is Eq. 2 when $V >> 0$.

A distribution of $(a-b)$ at different temperatures have been obtained from laboratory experiments for wet gabbro gouges[40]. We project this temperature-dependent $(a-b)$ distribution onto the slab interface using the thermal profile from a 2D steady-state thermal model constrained by P-wave seismic tomography in central Mexico[41]. We assume a downdip transition temperature, $(a-b)$ = 0, of 415^{o}C,

Table 1. Physical parameters used in the quasi-dynamic slow-slip cycle simulations.

Parameter	Symbol
rate-and-state direct effect parameter[a]	a
rate-and-state evolution effect parameter	b
characteristic slip distance (for SSEs)	D_{RS}^{SSE}
characteristic slip distance (for earthquakes)[b]	D_{RS}^{dy}
reference slip rate	v_0
reference friction coefficient	f_0
initial slip rate	V_{ini}
initial state variable	θ_{ini}
critical nucleation size	h_{RA}^*
quasi-static process zone size	Λ_0
effective normal stress	$\bar{\sigma}_n$
SSE effective normal stress	$\sigma_n^{\bar{S}SE}$
lithostatic pressure	σ_z
pore fluid pressure	p_f
rock density	ρ
shear modulus	μ
Poisson's ratio	ν

[a]Parameter a varies between velocity-weakening to velocity-strengthening [b] Our SSE cycle simulations do not incl

which coincides with the maximum down-dip extent of long-term SSEs inferred from GPS inversions[26]. Velocity-strengthening conditions $(a-b) > 0$ are imposed at the two lateral sides of the model domain to stabilize slip towards the plate convergence rate. The distribution of $(a-b)$ across the entire slab is shown in Figure S1a. The physical parameters including friction, initial stress and elastic material properties aforementioned are listed in Table S1.

3D SSE-initiated dynamic rupture models for the Guerrero earthquake

We use the open-source software *SeisSol* (https://github.com/SeisSol), which is based on the Arbitrary High-order Derivative (ADER) Discontinuous Garlekin (DG) finite element method, to perform simulations of earthquake rupture dynamics and seismic wave propagation[19–21]. *SeisSol* has been optimized for modern high-performance computing architectures including an efficient local time-stepping algorithm[22–25] and has been validated against several community benchmarks following the SCEC/USGS Dynamic Rupture Code Verification exercises[26,27]. Stress and particle velocities are approximated with 3rd-degree polynomials, yielding 4th-order accuracy in space and time during wave propagation simulation. We detail all dynamic rupture modeling parameters in the following.

Dynamic rupture initial stresses

We constrain the initial stresses in the dynamic rupture model from a snapshot of the shear and effective normal stresses across the fault interface in the 2014 SSE model. We track the traction ratio as the slow-slip fronts migrate along-strike and find that the local peak in the hypocentral region appears on day 317 (Fig. 2). This local peak of traction ratio is associated with the acceleration of the migrating front from 0.5 km/day to 3 km/day (Fig. 3c). The shear traction and effective normal stress on day 317 of the 2014 SSE quasi-dynamic model are saved and spatially interpolated onto the higher-resolution dynamic rupture mesh of the subduction fault surface using the package ASAGI[28]. The resulting ratio between the initial shear and effective normal stress is shown in Fig. 2. The time-dependent evolution of the traction ratio parameter on the fault during the modeled SSE is shown in Movie S2.

Velocity structure

We use a 1D depth-dependent model of the density and seismic velocities to set the elastic properties (μ and λ) in the dynamic rupture model, as shown in Fig. S6 and 1b. This 1D velocity model is based on seismic imaging of the central Mexico subduction zone[79] using the Mapping the Rivera Subduction Zone (MARS) seismic array, which consists of 50 broadband seismic instruments with a station spacing of ∼40 km deployed from January 2006 to June 2007. This 1D layered velocity structure captures the major features of the subsurface[31,31].

Linear slip-weakening friction

In the dynamic rupture simulations, we adopt a linear slip-weakening (LSW) friction law to constrain the fault frictional strength which has been shown to largely depend on the fault slip distance in laboratory experiments[32,33]. LSW friction laws have been widely used in dynamic rupture simulations including models of large megathrust earthquakes such as the 2004 M_w 9.1-9.3 Sumatra–Andaman earthquake[15,24], 2011 M_w 9.0 Tohoku-Oki earthquake[35], and rupture scenarios for the Cascadia subduction zone[38].

The LSW friction law is parameterized by the static (μ_s) and dynamic (mu_d) friction coefficients, critical slip-weakening distance (d_c), and frictional cohesion c_0. These initial conditions are difficult to constrain on the scale of megathrust slip, but play an important role in dynamic rupture nucleation and propagation[15,36]. Based on several trial dynamic rupture scenarios we set the static friction coefficient to

μ_s=0.626 and the dynamic friction coefficient to μ_d=0.546 within the assigned rupture asperities which yield realistic co-seismic rupture dynamics and arrest as well as spontaneous nucleation at a depth of 22 km due to the 2014 SSE stressing. Our choice of static friction allows for a smooth nucleation process at the hypocenter without introducing additional overstress, and is within the range of effective static friction typically used in dynamic rupture megathrust scenarios[35,51,67].

In our preferred model (referred to as Model A1), we include two asperities. We use a constant μ_d within each asperity. An increase in μ_d outside the asperities is required to allow a smooth and spontaneous rupture arrest. We increase μ_d outside the asperities using an exponential function in space $G_1(r_1, r_2)$:

$$G_1(r_1,r_2) = \begin{cases} min(1.0, \frac{1}{0.75} min(0.75, \exp(\frac{r_1^2}{r_1^2 - r_{c1}^2})) + \frac{1}{0.75} min(0.75, \exp(\frac{r_2^2}{r_2^2 - r_{c2}^2})) & r_1 \le r_{c1}, r_2 \le r_{c2} \\ 0.0 & otherwise \end{cases} \tag{6}$$

where r_i is defined as the epicentral distance from the center of each asperity $r_i = \sqrt{(x-x_{0i})^2 + (y-y_{0i})^2}, i = 1,2$. The radii of both asperities r_{c1}, r_{c2}, are chosen as 38 km and 42 km, respectively. The locations of their centers (x_{0i} and y_{0i}) are listed in Supplementary Table S4 and the distribution of G_1 is shown in Figure S8.

We find that by increasing μ_d to values 30% ($\mu_d = 0.826$) higher than μ_s, dynamic rupture gradually stops at the edges of the asperities. This setup results in a comparable duration and peak of moment release to teleseismic inversion[54] (Fig. 5a). The on-fault distribution of μ_d following $0.826 - 0.28 \times G_1(r_1, r_2)$ is shown in Figure 5f.

The critical slip distance d_c is generally not well constrained by seismic observations, for example, because of strong trade-offs with the assumed yield strength[40], limited near-field strong ground motion observations[1], and fault zone heterogeneity[35,42,50]. The choice of d_c also determines critical nucleation size and the required numerical on-fault resolution constrained by the process zone width[83,84]. Here, we use a relatively small and uniform critical slip-weakening distance of d_c=0.05 m which leads to realistic final slip, seismic stress drop, moment, and time-dependent moment release of the SSE-initiated dynamic

Table 2. Linear slip-weakening friction parameters used in the dynamic earthquake rupture simulations.

Parameter	Symbol	distribution	Value
static friction coefficient	μ_s	uniform	0.626
dynamic friction coefficient	μ_d	two asperities	0.546
critical slip distance	d_c	uniform	0.05 m
frictional cohesion	c_0	depth-dependent	1.0 - 0 MPa

rupture scenarios. We choose this slip-weakening critical distance since it allows for SSE-initiated large earthquake rupture and is at the lower limit of estimates from seismological observations[1] and at the upper limit of laboratory inferred estimates ($10^{-5} - 10^{-3}$ m)[2]. In an alternative model using d_c =0.5 m (not shown), dynamic rupture arrests quickly after the nucleation phase (Supplementary Information Text S2; Fig.S16).

It is difficult to observationally constrain the frictional cohesion c_0 of natural faults. In dynamic simulations, c_0 is typically assumed as 0.4 - 1.0 MPa at seismogenic depths and as high as 4-8 MPa at shallow depths to prevent large shallow slip or localized near-surface super-shear rupture speeds[43,51]. Here, we set $c_0 = 1.0$ MPa at depths shallower than 6.5 km and linearly decrease c_0 to 0 MPa at a depth of 10 km. All linear slip-weakening friction parameters (μ_s, μ_d, d_c, c_0) are listed in Table S2.

Alternative dynamic models with varying asperities

Our preferred dynamic rupture scenario includes two frictional asperities, which vary in their local dynamic friction coefficient from the surrounding slab interface, as proxies of megathrust heterogeneity governing the co-seismic rupture complexity. In the following, we show two selected alternative dynamic rupture scenarios that illustrate the sensitivity of our SSE-initiated co-seismic rupture dynamics to prescribed frictional asperities.

Model A2: two rupture asperities with higher initial shear stress

In dynamic rupture simulations, asperities due to locally reduced dynamic frictional strength lead to similar rupture behavior as asperities of elevated initial shear stress due to the equivalent fracture energy[39]. Here, we present an alternative dynamic rupture model, Model A2, with a constant dynamic friction coefficient but heterogeneous initial shear stress. The initial shear stress is smoothly reduced outside both rupture asperities, which leads to spontaneous rupture arrest. We use the same spatial exponential function $G_1(r_1, r_2)$ defined in Section 4 to decrease shear stresses smoothly outside the two geometrically equivalent pre-assigned rupture asperities. We set the initial shear stress as $\tau_0^{A2} = \tau_{SSE} \times G_1(r_1, r_2)$ where τ_{SSE} refers to the on-fault shear stress linked from the SSE cycle model (Fig. S10a). This setup leads to a localized distribution of the shear-to-effective-normal-stress ratio near the USGS catalog hypocenter (Fig. S10b).

The modeled source characteristics of the earthquake, including moment release, magnitude, slip distribution, and surface deformation, are all similar to our preferred model (Fig.S12), except for a slightly sharper peak in moment release, corresponding to rupture arrest, than that of our preferred model (Model A1). We conclude that, in principle, local shear-stress asperities can lead to equivalent SSE-initiated rupture dynamics compared to frictionally-weak asperities.

4.1 Model B1: a single rupture asperity with reduced dynamic friction coefficient μ_d

Next, we demonstrate the sensitivity of rupture dynamics and synthetic observables (e.g., moment rate release) to megathrust heterogeneity using a single circular asperity wherein the dynamic frictional strength locally decreases (Model B1; Figure SS9a). We use a spatial exponential function (G_2) that contains a single asperity to manipulate the dynamic friction coefficient (Fig. S9a) (Supplementary Information Text S2).

The resulting moment magnitude is only $M_\mathrm{w}7.15$, and the moment rate release features a single sharp peak instead of reproducing the observed characteristic two-peak shape (Fig. S9c). The modeled spatial extents of the fault slip and surface displacement amplitudes are significantly smaller (Fig. S9b,c,d).

Fracture energy and stress drop

Fracture energy, defined as the strain energy consumed during shear sliding using the framework of linear elastic fracture mechanics, has been closely linked to fault-weakening mechanisms[58,60]. In dynamic rupture simulations governed by linear slip-weakening friction, we can calculate fracture energy as follows:

$$G_c = \frac{(\tau_y - \tau_d)d_c}{2}, \tag{7}$$

where G_c is the fracture energy, τ_y denotes the frictional yielding strength and τ_d is the dynamic residual shear stress at a specific location on the fault.

We estimate the average fracture energy during the initial stage of dynamic rupture E_{nu} using :

$$\bar{G}_{nu} = \frac{\int_{\Sigma_{nu}}(\tau_y - \tau_d)\frac{d_c}{2}d\Sigma_{nu}}{\int_{\Sigma_{nu}} s_i d\Sigma_{nu}}. \tag{8}$$

where Σ_{nu} is the effective nucleation area, defined as the elements where the SSE-induced initial shear stress τ_0 overcomes the assumed frictional strength τ_y. s_i denotes the area of the element i.

We calculate the total fracture energy (E_G) by integrating over elements on the fault for which the final slip distance $\delta_{final} \geq d_c$:

$$E_G = \int_{\Sigma}(\tau_y - \tau_d)\frac{d_c}{2}d\Sigma. \tag{9}$$

where τ_d and $\delta_f(x)$ refer to the final stress and slip on the rupture area (Σ), respectively, where the final slip is larger than d_c =0.05 m.

The average fracture energy $\bar{G_c}$ is defined as the average of the selected rupture area as

$$\bar{G_c} = \frac{E_G}{\int_{\Sigma} s_i d\Sigma}, \tag{10}$$

where s_i is the area of the element i.

Stress drop can be defined as the difference between the dynamic rupture initial and residual shear stresses. We calculate the average stress drop across the rupture area using two methods:

1. as a spatially averaged stress drop $\overline{\triangle\tau_A}$ defined as

$$\overline{\triangle\tau_A} = \frac{\int_{\Sigma}\triangle\tau d\Sigma}{\int_{\Sigma} d\Sigma}, \tag{11}$$

where $\overline{\triangle\tau_A}$, $\triangle\tau$ and Σ represent spatially-averaged stress drop, local stress drops and rupture areas across the fault, respectively;

2. as an average stress drop based on energy considerations[55,56] as

$$\overline{\triangle\tau_E} = \frac{\int_\Sigma \triangle\tau\delta_f(x)d\Sigma}{\int_\Sigma \delta_f(x)d\Sigma}, \tag{12}$$

where $\overline{\triangle\tau_E}$ is the energy-based stress drop, and $\delta_f(x)$ is the accumulated total slip at each point x of the fault.

model	initial shear stress	dynamic friction coefficient μ_d	resulting magnitude
Model A1	SSE	two asperities	M_w 7.28
Model A2	SSE + two asperities	uniform	M_w 7.25
Model B1	SSE	one asperity	M_w 7.15

Table 3. Varying dynamic rupture model parameters (initial shear stress, dynamic friction coefficient) and resulting moment magnitudes.

i	x_i (m)	y_i (m)
1	-18950.0	-84000.0
2	-59630.0	-73350.0

Table 4. Cartesian coordinates of the locations of the centers of the circular asperities (r_i). These are used in the exponential shape function $G1(r_1, r_2$
which has been defined in Section 4.

4.2 Fault geometry and computational meshes

We build the model using the slab geometry inferred from the Middle America Seismic Experiment (MASE)[28] (Fig. 1b). MASE provided high-resolution upper continental structure of the central Mexican subduction using routine methods, including receiver functions and seismic velocity tomography. The fault geometry is constructed from inferred depth contours with a depth-spacing of 5 km and smoothed slightly to avoid potential numerical artifacts, such as, caused by abrupt changes in dip angles. We use the standard global projection WGS84/UTM, zone 11N to Cartesian coordinates.

We use the same fault geometry but different spatial extents and resolutions of the computational meshes in the SSE and dynamic rupture simulations, to ensure adequate resolution. In the SSE model, we discretize the 450 km-long and 55 km deep slab interface into triangular elements of no more than 1,500 m edge length using the commercial software Trelis (https://csimsoft.com/trelis). The slow-slip cycle models require $\sim$10 h on 1536 cores for a 250-year-long SSE simulation on SuperMUC-NG at the Leibniz Supercomputing Centre in Garching, Germany.

For the dynamic rupture simulations, we focus on a sub-region of a length of 200 km along-strike. The rupture area of the M_w 7.3 Guerrero earthquake (Fig. 1a) is smaller than the 450 km-long fault used for the SSE cycle model. We use the same slab geometry but additionally add topography during the generation of a volumetric tetrahedral mesh suitable for dynamic rupture earthquake simulations with

SeisSol (Fig. 1b)). We incorporate topography data at 1-arc-minute spatial resolution from the *ETOPO1* model (https://www.ngdc.noaa.gov/mgg/global/) in a cubic domain of 500 km $\times$ 500 km $\times$ 200 km which is large enough to avoid any spurious reflected waves from the sides and bottom of the model domain.

It is crucial to ensure sufficiently high on-fault resolution to resolve the dynamic process zone[49], the width of which varies in space and time, and with the initial conditions that affect the total available fracture energy and rupture velocity[84]. For our preferred dynamic rupture scenario, we measure the average size of the dynamic process zone to be $\sim$1800 m. We choose slab interface element edge lengths of no more than 400 m, which is sufficient to resolve the process zone in our 4th-order accurate simulations[83,84]. The volumetric tetrahedral mesh is generated using SimModeler from *SimMetrix* (http://www.simmetrix.com/), which is free for academic use. The mesh is coarsened based on the distance normal to the fault surface at a graduation rate of 0.3, reducing the resolution for outgoing seismic waves for efficiency. The topographic surface is discretized using triangles of at most $\sim$2,000 m in length. Our resulting mesh for all shown dynamic rupture simulations consists of 11,764,144 elements in total. All simulations were performed on SuperMUC-NG at the Leibniz Supercomputing Centre in Garching, Germany. A simulation of 4th-order accuracy for 90 s duration requires 2800 CPU hours.

References in Methods

1. Mikumo, T., Olsen, K. B., Fukuyama, E. & Yagi, Y. Stress-breakdown time and slip-weakening distance inferred from slip-velocity functions on earthquake faults. *Bull. Seism. Soc. Am.* **93**, 264–282, DOI: 10.1785/0120020082 (2003).

2. Marone, C. Laboratory-derived friction laws and their application to seismic faulting. *Annu. Rev. Earth Planet. Sci.* **26**, 643–696 (1998).

3. Rice, J. R. Spatiotemporal complexity of slip on a fault. *J. Geophys. Res.* **98**, 9885–9907, DOI: 10.1029/93JB00191 (1993).

4. Stuart, W. D., Hildenbrand, T. G. & Simpson, R. W. Stressing of the New Madrid Seismic Zone by a lower crust detachment fault. *J. Geophys. Res.* **102**, DOI: 10.1029/97jb02716 (1997).

5. DeMets, C., Gordon, R. G. & Argus, D. F. Geologically current plate motions. *Geophys. J. Int.* **181**, 1–80, DOI: 10.1111/j.1365-246X.2009.04491.x (2010).

6. Jiang, J. *et al.* Community-driven code comparisons for three-dimensional dynamic modeling of sequences of earthquakes and aseismic slip. *J. Geophys. Res.* **127**, e2021JB023519, DOI: https://doi.org/10.1029/2021JB023519 (2022).

7. Erickson, B. A. *et al.* Incorporating full elastodynamic effects and dipping fault geometries in community code verification exercises for simulations of earthquake sequences and aseismic slip (seas). *Bull. Seism. Soc. Am.* DOI: 10.1785/0120220066 (2023).

8. Lapusta, N. & Liu, Y. Three-dimensional boundary integral modeling of spontaneous earthquake sequences and aseismic slip. *J. Geophys. Res.* **114**, DOI: 10.1029/2008JB005934 (2009).

9. Thomas, M. Y., Lapusta, N., Noda, H. & Avouac, J.-P. Quasi-dynamic versus fully dynamic simulations of earthquakes and aseismic slip with and without enhanced coseismic weakening. *J. Geophys. Res. Solid Earth* **119**, 1986–2004, DOI: https://doi.org/10.1002/2013JB010615 (2014). https://agupubs.onlinelibrary.wiley.com/doi/pdf/10.1002/2013JB010615.

10. Dieterich, J. H. Modeling of rock friction 1. Experimental results and constitutive equations. *J. Geophys. Res* **84**, 2161–2168, DOI: 10.1029/JB084iB05p02161 (1979).

11. Ruina, A. L. Slip instability and state variable friction laws. *J. Geophys. Res.* **88**, 10359–10370, DOI: 10.1029/JB088iB12p10359 (1983).

12. Rubin, A. M. & Ampuero, J.-P. Earthquake nucleation on (agine) rate and state faults. *J. Geophys. Res.* **110**, DOI: 10.1029/2005JB003686 (2005).

13. Liu, Y. & Rice, J. R. Slow slip predictions based on granite and gabbro friction data compared to GPS measurements in northern Cascadia. *J. Geophys. Res.* **114**, DOI: 10.1029/2008JB006142 (2009).

14. Day, S. M., Dalguer, L. A., Lapusta, N. & Liu, Y. Comparison of finite difference and boundary integral solutions to three-dimensional spontaneous rupture. *J. Geophys. Res.* **110**, DOI: 10.1029/2005jb003813 (2005).

15. Beeler, N. M., Tullis, T. E., Blanpied, M. L. & Weeks, J. D. Frictional behavior of large displacement experimental faults. *J. Geophys. Res.* **101**, 8697–8715 (1996).

16. Rice, J. R. & Ben-Zion, Y. Slip complexity in earthquake fault models. *Proc. Natl. Acad. Sci.* **93**, 3811–3818 (1996).

17. He, C., Wang, Z. & Yao, W. Frictional sliding of gabbro gouge under hydrothermal conditions. *Tectonophys.* **445**, 353–362, DOI: 10.1016/j.tecto.2007.09.008 (2007).

18. Manea, V. C. & Manea, M. Flat-slab thermal structure and evolution beneath central mexico. *Pure Appl. Geophys.* **168**, 1475–1487, DOI: 10.1007/s00024-010-0207-9 (2011).

19. Käser, M. & Dumbser, M. An arbitrary high-order discontinuous galerkin method for elastic waves on unstructured meshes - i. the two-dimensional isotropic case with external source terms. *Geophys. J. Int.* **166**, 855–877, DOI: 10.1111/j.1365-246X.2006.03051.x (2006).

20. Dumbser, M. & Käser, M. An arbitrary high-order discontinuous galerkin method for elastic waves on unstructured meshes - ii. the three-dimensional isotropic case. *Geophys. J. Int.* **167**, 319–336, DOI: 10.1111/j.1365-246X.2006.03120.x (2006).

21. Pelties, C., de la Puente, J., Ampuero, J.-P., Brietzke, G. B. & Käser, M. Three-dimensional dynamic rupture simulation with a high-order discontinuous galerkin method on unstructured tetrahedral meshes. *J. Geophys. Res.* **117**, DOI: doi:10.1029/2011JB008857 (2012).

22. Breuer, A. *et al.* Sustained petascale performance of seismic simulations with seissol on supermuc. In *International Supercomputing Conference*, 1–18 (Springer, 2014).

23. Heinecke, A. *et al.* Petascale high order dynamic rupture earthquake simulations on heterogeneous supercomputers. In *SC '14: Proceedings of the International Conference for High Performance Computing, Networking, Storage and Analysis*, 3–14, DOI: 10.1109/SC.2014.6 (2014).

24. Uphoff, C. *et al.* Extreme scale multi-physics simulations of the tsunamigenic 2004 sumatra megathrust earthquake, DOI: 10.1145/3126908.3126948 (2017).

25. Krenz, L. *et al.* 3D Acoustic-Elastic Coupling with Gravity: The Dynamics of the 2018 Palu, Sulawesi Earthquake and Tsunami. In *The International Conference for High Performance Computing, Net-*

working, Storage and Analysis, SC '21, DOI: 10.1145/3458817.3476173 (Association for Computing Machinery, 2021).

26. Pelties, C., Gabriel, A. A. & Ampuero, J. P. Verification of an ader-dg method for complex dynamic rupture problems. *Geosci. Model. Dev.* **7**, 847–866, DOI: 10.5194/gmd-7-847-2014 (2014).

27. Harris, R. A., Barall, M., Aagaard, B. T., Ma, S. & Daniel Roten, e. a., Kim B. Olsen. A suite of exercises for verifying dynamic earthquake rupture codes. *Seism. Res. Lett.* **89**, 1146–1162, DOI: 10.1785/0220170222 (2018).

28. Rettenberger, S., Meister, O., Bader, M. & Gabriel, A.-A. Asagi: A parallel server for adaptive geoinformation. In *Proceedings of the Exascale Applications and Software Conference 2016*, EASC '16, DOI: 10.1145/2938615.2938618 (Association for Computing Machinery, New York, NY, USA, 2016).

29. Dougherty, S. L. & Clayton, R. W. Seismicity and structure in central mexico: Evidence for a possible slab tear in the south cocos plate. *J. Geophys. Res.* **119**, 3424–3447, DOI: 10.1002/2013jb010883 (2014).

30. Song, T. R. *et al.* Subducting slab ultra-slow velocity layer coincident with silent earthquakes in southern mexico. *Science* **324**, 502–6, DOI: 10.1126/science.1167595 (2009).

31. Kim, Y., Clayton, R. W. & Jackson, J. M. Geometry and seismic properties of the subducting cocos plate in central mexico. *J. Geophys. Res.* **115**, DOI: doi:10.1029/2009JB006942 (2010).

32. Ida, Y. Cohesive force across the tip of a longitudinal-shear crack and griffith's specific surface energy. *J. Geophys. Res.* **77**, 3796–3805 (1972).

33. Palmer, A. C. & Rice, J. R. The growth of slip surfaces in the progressive failure of over-consolidated clay. *Proc. Royal Soc. London. A. Math. Phys. Sci.* **332**, 527–548 (1973).

34. Ulrich, T., Gabriel, A.-A. & Madden, E. H. Stress, rigidity and sediment strength control megathrust earthquake and tsunami dynamics. *Nat. Geosci.* **15**, 67–73, DOI: 10.1038/s41561-021-00863-5 (2022).

35. Galvez, P., Ampuero, J.-P., Dalguer, L. A., Somala, S. N. & Nissen-Meyer, T. Dynamic earthquake rupture modelled with an unstructured 3-d spectral element method applied to the 2011 m 9 tohoku earthquake. *Geophys. J. Int.* **198**, 1222–1240 (2014).

36. van Zelst, I., Wollherr, S., Gabriel, A.-A., Madden, E. H. & van Dinther, Y. Modeling megathrust earthquakes across scales: One-way coupling from geodynamics and seismic cycles to dynamic rupture. *J. Geophys. Res. Solid Earth* **124**, 11414–11446, DOI: https://doi.org/10.1029/2019JB017539 (2019).

37. Ramos, M. D. & Huang, Y. How the transition region along the cascadia megathrust influences coseismic behavior: Insights from 2-d dynamic rupture simulations. *Geophys. Res. Lett.* **46**, 1973–1983 (2019).

38. Madden, E. H., Ulrich, T. & Gabriel, A.-A. The state of pore fluid pressure and 3-d megathrust earthquake dynamics. *J. Geophys. Res.* **127**, e2021JB023382, DOI: https://doi.org/10.1029/2021JB023382 (2022).

39. Ye, L., Lay, T., Kanamori, H. & Rivera, L. Rupture characteristics of major and great ($m_w \leq 7.0$) megathrust earthquakes from 1990 to 2015: 2.depth dependence. *J. Geophys. Res.* **121**, 845–863, DOI: 10.1002/2015jb012427 (2016).

40. Guatteri, M. & Spudich, P. What can strong-motion data tell us about slip-weakening fault-friction laws? *Bull. Seismol. Soc. Am.* **90**, 98–116 (2000).

41. Collettini, C., Tesei, T., Scuderi, M., Carpenter, B. & Viti, C. Beyond byerlee friction, weak faults and implications for slip behavior. *Earth Planet. Sci. Lett.* **519**, 245–263, DOI: https://doi.org/10.1016/j.epsl.2019.05.011 (2019).

42. Gallovic, F., Valentová, Ĺ., Ampuero, J.-P. & Gabriel, A.-A. Bayesian dynamic finite-fault inversion: 2. application to the 2016 mw 6.2 amatrice, italy, earthquake. *J. Geophys. Res. Solid Earth* **124**, 6970–6988, DOI: https://doi.org/10.1029/2019JB017512 (2019).

43. Wollherr, S., Gabriel, A.-A. & Mai, P. M. Landers 1992 "reloaded": Integrative dynamic earthquake rupture modeling. *J. Geophys. Res.* **124**, 6666–6702, DOI: https://doi.org/10.1029/2018JB016355

(2019).

44. Tinti, E. *et al.* Constraining families of dynamic models using geological, geodetic and strong ground motion data: The mw 6.5, october 30th, 2016, norcia earthquake, italy. *Earth Planet. Sci. Lett.* **576**, DOI: 10.1016/j.epsl.2021.117237 (2021).

45. Abercrombie, R. E. & Rice, J. R. Can observations of earthquake scaling constrain slip weakening? *Geophys. J. Int.* **162**, 406–424 (2005).

46. Tinti, E., Spudich, P. & Cocco, M. Earthquake fracture energy inferred from kinematic rupture models on extended faults. *J. Geophys. Res.* **110**, DOI: 10.1029/2005jb003644 (2005).

47. Noda, H., Lapusta, N. & Kanamori, H. Comparison of average stress drop measures for ruptures with heterogeneous stress change and implications for earthquake physics. *Geophys. J. Int.* **193**, 1691–1712, DOI: 10.1093/gji/ggt074 (2013).

48. Perry, S. M., Lambert, V. & Lapusta, N. Nearly magnitude-invariant stress drops in simulated crack-like earthquake sequences on rate-and-state faults with thermal pressurization of pore fluids. *J. Geophys. Res.* **125**, e2019JB018597, DOI: https://doi.org/10.1029/2019JB018597 (2020).

49. Day, S. M. Three-dimensional simulation of spontaneous rupture: the effect of nonuniform prestress. *Bull. Seismol. Soc. Am.* **72**, 1881–1902 (1982).

50. Wollherr, S., Gabriel, A.-A. & Uphoff, C. Off-fault plasticity in three-dimensional dynamic rupture simulations using a modal discontinuous galerkin method on unstructured meshes: implementation, verification and application. *Geophys. J. Int.* **214**, 1556–1584, DOI: 10.1093/gji/ggy213 (2018).

Acknowledgements

This work was supported by the European Research Council (ERC) under the European Union's Horizon 2020 research and innovation programme (TEAR, Grant agreement No. 852992). The authors acknowledge additional support by the National Science Foundation (Grant No. EAR-2121666), the National Aeronautics and Space Administration (80NSSC20K0495), and Horizon Europe (ChEESE-2P grant agreement No. 101093038, DT-Geo grant agreement No. 101058129, and Geo-Inquire grant agreement No. 101058518). Computing resources were provided by the Leibniz Supercomputing Centre (LRZ, project No. pr63qo and No. pr49ha on SuperMUC-NG) and by the Institute of Geophysics of LMU Munich[85]. We thank Andrea Perez-Silva for a number of initial tests during her Master thesis. We thank Dr. Mathilde Radiguet for kindly sharing the GPS inversion results of the Guerrero slow slip event. We appreciate the fruitful discussion with Dr. Yoshihiro Kaneko, Dr. Luis Dalguer, and the seismology group at Munich University (LMU). We use TriBIE (https://github.com/daisy20170101/TriBIE) for the slow slip simulation and SeisSol Master branch, available on GitHub (github.com/SeisSol/SeisSol) for dynamic rupture simulation. How to download and run the code is described in the SeisSol documentation (seissol.readthedocs.io/en/latest/). We use the software SKUA-GOCAD (pdgm.com/products/skua-gocad/) as modeling environment to produce all 3D fault models. Earthquake source data of the 2014 Guerrro event is from USGS (https://earthquake.usgs.gov/earthquakes/eventpage/usb000pq41/executive) and GCMT (https://www.globalcmt.org). All input files and meshes required to reproduce the TriBIE long-term slow slip cycle and SeisSol earthquake dynamic rupture scenarios can be downloaded from https://doi.org/10.5281/zenodo.6956697.

Author contributions statement

Conceptualization: D.L., A.-A.G. Formal Analysis: D.L. Funding Acquisition: A.-A.G. Investigation: D.L. Methodology: D.L., A.-A.G. Project Administration: A.-A.G. Resources: A.-A.G. Software: D.L., A.-A.G. Supervision: A.-A.G. Visualization: D.L. Writing – Original Draft Preparation: D.L., A.-A.G. Writing – Review and Editing: D.L., A.-A.G.